International Journal of Greenhouse Gas Control 109 (2021) 103376

Contents lists available at ScienceDirect

International Journal of Greenhouse Gas Control

journal homepage: www.elsevier.com/locate/ijggc

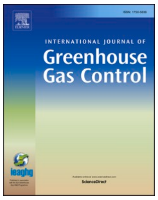

The role of mechanical stratigraphy on CO_2 migration along faults – examples from Entrada Sandstone, Humbug Flats, Utah, USA

E. Skurtveit [a,b,*], A. Torabi [b], A. Sundal [b], A. Braathen [b]

[a] Norwegian Geotechnical Institute, Oslo, Norway
[b] Department of Geosciences, University of Oslo, Oslo, Norway

ARTICLE INFO

Keywords:
Faults
Mechanical properties
Stratigraphy
Fluid flow
CO_2 storage

ABSTRACT

Bleaching patterns along a faulted succession provides new insight into fluid migration pathways controlled by the fault zone and mechanical stratigraphy. In order to investigate this effect, we logged stratigraphic layers in Humbug Flats, Utah, USA both in host rocks and faulted rocks, where a 40 m offset normal fault cuts through the Entrada Sandstone. We measured petrophysical and mechanical properties using TinyPerm II, Schmidt Hammer and laboratory core testing for selected layers. Bleaching has been identified as a proxy for fluid migration parallel to bedding, which fades out with distance from faults. A new observation is that fracturing of bed interfaces contributes to horizontal flow out from the fault zone. Longer-distance comprehensive bleaching dominates the most permeable beds (units), hosting porosity-controlled deformation band associated to fault zones. Fractures prevail in low permeability and stiffer units, where isolated fracture parallel bleaching haloes are observed within fault damage and process zones. Strong correlation is observed between permeability/porosity and stiffness/strength properties for the tested samples of different layers along the stratigraphic logs. For the studied fault, fractures provide important conduits for vertical flow across low permeability and stiff layers, whereas the more porous layers provide bedding-parallel flow paths out of the fault zone.

1. Introduction

For centuries fluid flow in faulted sedimentary basins has been difficult to forecast (Faulkner et al., 2010). Assessment of leakage risk of CO_2 associated with faults is currently conducted by industry state-of-the-art workflows for fault-seal analysis (e.g. Knipe, 1997), which mainly addresses across-fault flow and communication between reservoir compartments. Existing tools are developed based on extensive experience with hydrocarbon exploration and production identifying shale content along faults (e.g., Shale Gouge Ratio) as one controlling parameter for fault sealing (e.g. Pei et al., 2015). These proxies arguably describe elements of fault structure; however, the methodology cannot capture the complexity of fault core and damage zone independent of the presence of shale layers, nor the flow within or vertically along faults (Braathen et al., 2009; Fachri et al., 2016; Faille et al., 2014). The potential for faults to act as vertical conduits is highly relevant for injection operations like CO_2 storage, wastewater injection and reservoir pressure support. This challenge calls for more detailed mapping of the mechanical stratigraphy influencing the structural style of the fault (Ferrill et al., 2017) and the vertical fluid migration pathways like fracture corridors (Lunn et al., 2008; Ogata et al., 2014).

Studies of exhumed reservoirs showing evidence of fluid transport in geological history offer a unique possibility to supplement our knowledge of fluid migration pathway along faults and fracture corridors as well as understand interrelationships between observed bleaching patterns and geomechanical stratigraphy. Migration of CO_2- and/or CH_4-rich groundwaters as well as H_2S causes bleaching (i.e. reduction of Fe (III) and/or dissolution of Fe-oxides) of aeolian sandstone (reservoir) and siltstone (seal) layers which were originally stained red by haematite or goethite (e.g. Beitler et al., 2005; Chan et al., 2000; Eichhubl et al., 2009; Garden et al., 2001; Kampman et al., 2016; Wigley et al., 2012), and hints at preferential flow paths such as permeable layers, fault planes, and damage zones (i.e. by change from red to white colour). In distinctly red, Jurassic units of the San Rafael Swell area, Utah, these bleaching patterns are easily observed in the field and allow for identification of relict fluid pathways related to faults and fracture corridors (Ogata et al., 2014; Skurtveit et al., 2017; Sundal et al., 2017) and through fracture networks in the caprock (Petrie et al., 2014), identifying several episodes of fluid flow (Rushton et al., 2020). Mobility of the reducing fluids in Utah has been attributed to several events

---

* Corresponding author.
E-mail address: Elin.Skurtveit@ngi.no (E. Skurtveit).

https://doi.org/10.1016/j.ijggc.2021.103376
Received 27 November 2020; Received in revised form 26 May 2021; Accepted 1 June 2021

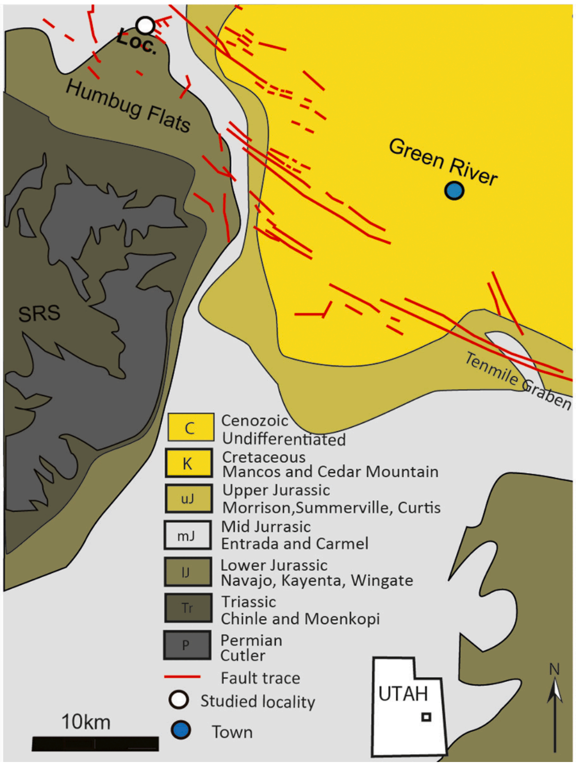

Fig. 1. Location of the Humbug Flats area near Green River Utah, USA. Modified from Doelling (2002) and Torabi et al. (2019a). The Entrada Sandstone distribution is shown as light grey.

interlinked with salt tectonics in the Paradox Basin and Laramide-style monocline growth of the San Rafael Swell (Kampman et al., 2014), whereas CO_2 appears sourced mainly from the mantle (e.g. Burnside et al., 2013; Frery et al., 2015). Previous work on Humbug Flats (Ogata et al., 2014; Torabi et al., 2019a, 2019b) have addressed the architecture of faults and their importance for fluid flow and bleaching patterns encountered in the Humbug Flats. Dissolution of haematite grain coats and carbonate cement in the Entrada Sandstone has been found to reduce fracture toughness with nearly 40% relative to unaltered samples (Major et al., 2018). This was also demonstrated by Espinoza et al. (2018), reporting a reduction in shear strength and stiffness in samples from the Entrada Sandstone during a limited number of triaxial tests, due to CO_2 fluid alteration. However, the data is limited and the effects of bleaching on petrophysical and geomechanical properties are still poorly understood. There are also open questions related to the timing of the bleaching, the types of fluids involved and implications for fluid migration pathways.

In this study, we present a dataset on mechanical and petrophysical properties of faulted sandstones from core plugs and field measurements using a TinyPerm II and a Schmidt Hammer type N, addressing permeability, stiffness and strength. The data collected within faulted Entrada Sandstone at Humbug Flats in Utah (Fig. 1) are compared with observed bleaching patterns and sedimentary characterization of the layers. Our aim is to analyse the correlations between porosity/permeability and stiffness/strength for bleached versus non-bleached samples and highlight the role of the sedimentary stratigraphy on the fluid migration pathways within and immediately outside the fault zone.

2. Geology

2.1. Stratigraphy and structural setting

The Humbug Flats area is located in the northeastern part of the San Rafael Swell (SRS), beyond the northwestern termination of the Paradox Basin (Fig. 1). SRS is defined by an east-verging, doubly-plunging monocline that trends NNE–SSW, with a northern tip in the study area. This km-amplitude structure formed during the Late Campanian–Eocene in the Laramide Orogeny (Bump and Davis, 2003), as one of many contractional fault-propagation folds (Bump and Davis, 2003; Davis and Bump, 2009) that formed above blind reverse faults. In its central region, the San Rafael Monocline is characterized by a sub-horizontal to gently dipping western backlimb and a steep to subvertical eastern forelimb.

Near the northern monocline tip, the Humbug Flats area locates to a gently curved anticline (Fig. 1). As the regional monocline bounds an array/set of faults in the region (e.g., Ogata et al., 2014), faulting is

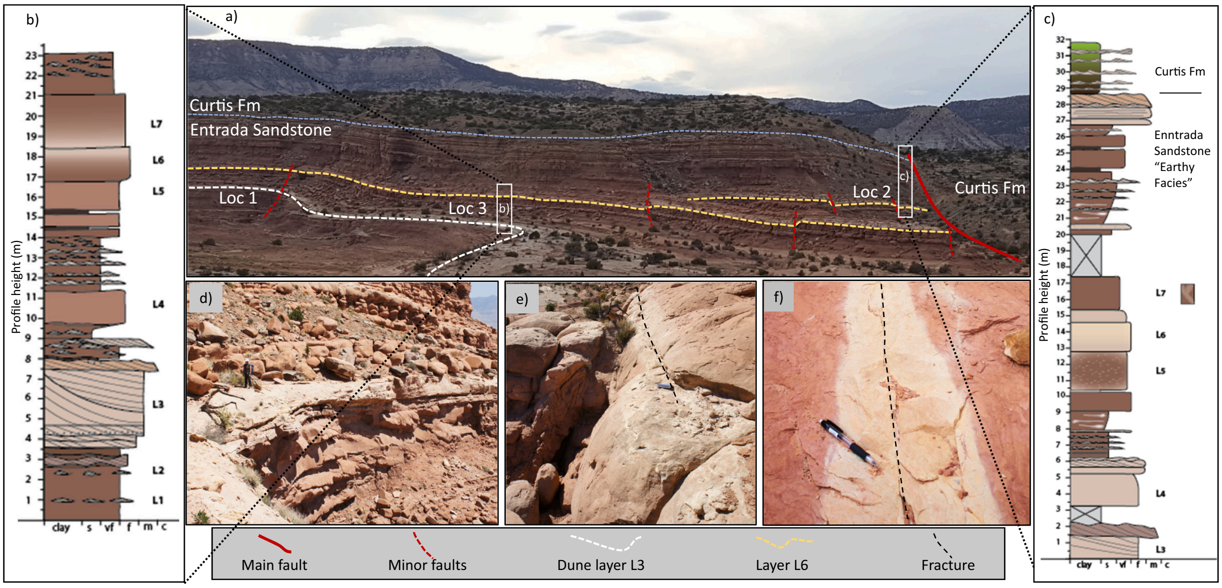

Fig. 2. a) Overview Entrada Sandstone and normal fault in Humbug Flats, with the three main study sites, location 1,2 and 3 marked. b) Sedimentary log from location 3 showing the layers L1-L7 in the reference position outside the fault zone. c) Sedimentary log from location 2 showing layer L3-L7 within the main fault damage zone. Detailed photographs are included for the 3 main bleaching features of interest, the white costal dune L3 in (d), layer parallel bleaching of L6 and L7 in (e) and bleached halo around fracture associated with minor faults in layer L1, location 1 in (f).

Table 1
Facies associations of layers in the lithomechanical succession studied based on detailed facies descriptions and sedimentology of the Entrada Sandstone earthy member in areas near the Humbug Flats (Bromander, 2018; Da Costa, 2018; Sundal et al., 2016).

Layer	Facies association	Grain size	Sedimentology
L6, L7	Aeolian dunes	vf-f	Wind transported sediment, deposited as through cross-bedded sand in dunes, appearing as massive beds. Pore filling and grain coating Fe-oxides.
L1, L2, L4, L5	Interdune and sabkha	clay-vf	Fine grained material deposited as wind-blown loess, mottled. Immature soil profiles and salt crusts. Sandy interlayers from fluvial channels and terminal splays. Pore filling and grain coating Fe-oxides.
L3	Coastal dunes	f-m	Sand dunes deposited at the coast and modified by shallow marine and tidal processes. High energy environment, low clay content.

considered temporal with growth of the San Rafael Monocline, but local stratigraphic control on timing is lacking. In the study area, one of these NW-SE trending NE-dipping normal faults truncate the gentle anticline, defining the most noticeable structure in the area. Fault displacement of around 40 m causes juxtaposition of the Entrada Sandstone with Curtis Formation in the hanging wall (Ogata et al., 2014; Torabi et al., 2019b). For the footwall damage zone of this fault, in the Entrada Sandstone, several small-scale faults, fractures and deformation bands as well as fracture corridors, comprising joint swarms and subordinate shear fractures are prominent in different stratigraphic layers. The damage zone has been divided into an inner damage zone of around 10 m followed by an outer damage zone stretching around 40 m out from the main fault (Torabi et al., 2019a) comprising several minor faults and the fault tip process zone.

2.2. Entrada sandstone in the humbug flats

The local stratigraphy is shown in Fig. 2 with the reservoir – seal succession of interest comprised of the upper part of Middle Jurassic Entrada Sandstone, overlain by the Curtis Formation. Location 1 is a minor, 1 m displacement, fault outside the main fault zone. Location 2 is within the main fault damage zone and location 3 is a reference position outside the fault zones (Fig. 2a). Sedimentary logs are presented for two sites, locations 2 and 3, comparing the stratigraphy within and outside the fault damage zone (Fig. 2b, c).

The upper part of the Entrada Sandstone, informally referred to as “earthy facies” (e.g. Zuchuat et al., 2019), was deposited in a wet aeolian environment, transitioning into (supra-) tidal to shallow marine settings. Sandy sediments were deposited as dunes, in bars, channels and splays, representing permeable reservoir units, whereas silt and mud was deposited in sabkha and interdune settings, providing low permeability fluid seals. Some fine-grained inter-dune deposits are locally bioturbated and appear as mottled with light blotches in sand lenses and around rootlets. Some distinct layers (L) with a pale white colour (bleached layers) stand out in the otherwise dominantly red-coloured stratigraphy (Fig. 2d and e). This includes units L3, L6 and partly L7. L3 is a dune layer with a pale white colour observed throughout the study area. L6 and L7 are found to be a silt-sand mix with local layer parallel bleaching fading out with distance from the main fault. Very prominent bleaching features in the area are the light “halos” around vertical to subvertical fractures within otherwise red coloured, low permeable units (Fig. 2f). This local bleaching indicates past circulation of a reducing fluid (e.g. Chan et al., 2000; Garden et al., 2001; Newell et al., 2019; Ogata et al., 2014; Parry et al., 2004).

Fe-oxides are associated with red staining of sediments and occur as pore-fill and grain coatings, but not directly acting as the main cementing agent, and with total amounts related to facies (Table 1). The variance in Fe-oxide contents are expected to be in the order of 0.2 - 1 wt.% (e.g. Beitler et al., 2005; Rushton et al., 2020) meaning that quantification of subtle changes and natural variation is difficult. The studied sandstone layers are primarily quartz arenite, except L3 that has

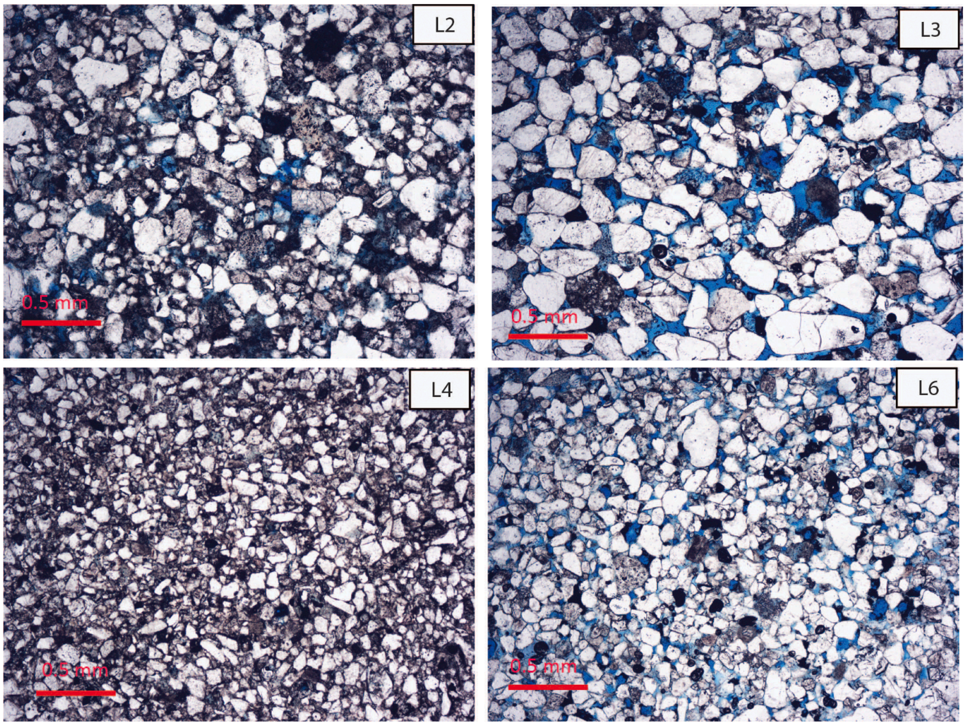

Fig. 3. Examples of microscopic structure of inherent red samples (L2, L4 and L6) and white layer (L3) with minimal inherent Fe-oxides. Note the coarser grain size and presence of open pores, indicating higher porosity in the L3 and L6 samples.

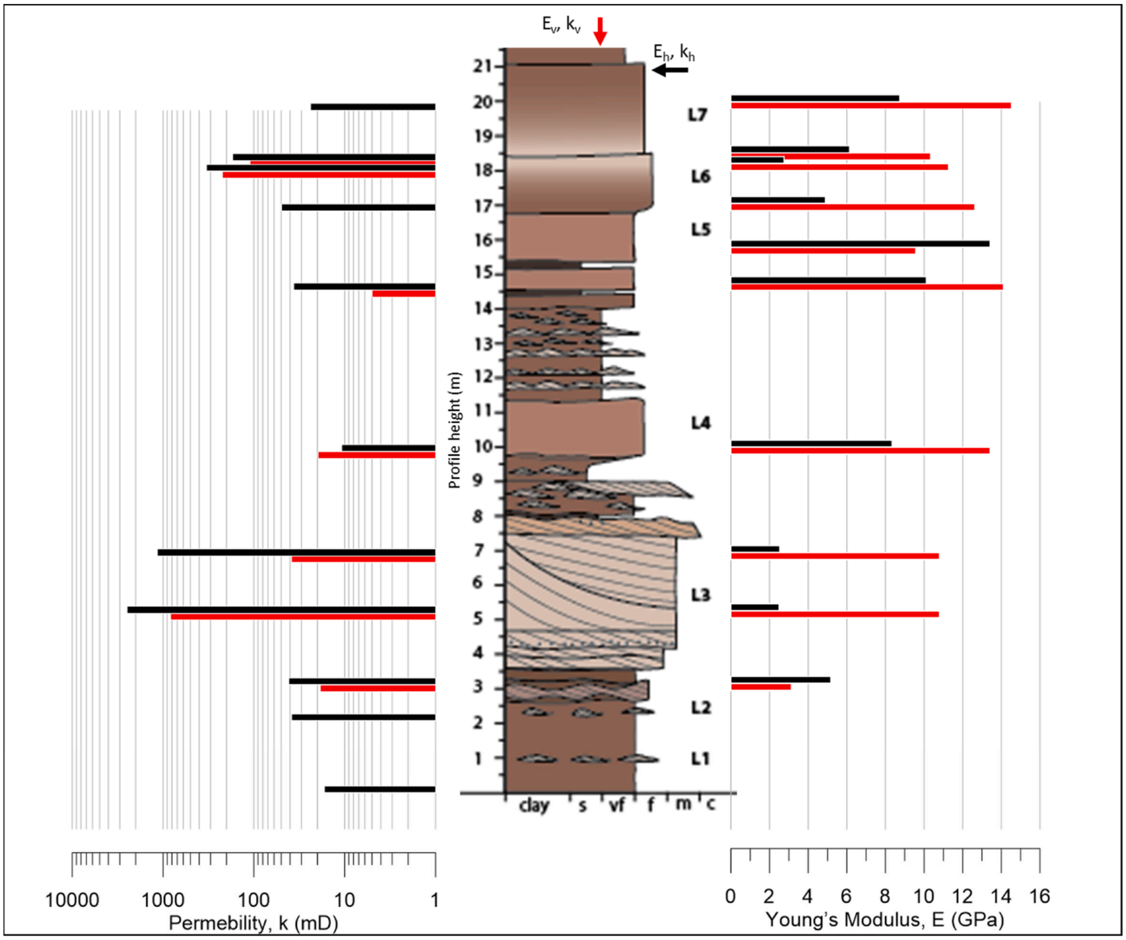

Fig. 4. Mechanical and petrophysical stratigraphy illustrated by Tiny-Perm II permeability and Young's Modulus from Schmidt hammer rock hardness measurements of layers L1-L7 from the reference location 3 outside the fault damage zone. Red columns are for vertical direction and black are for the horizontal direction as indicated on top of the sedimentary log.

slightly less quartz and higher K-feldspar content and is categorized as subarkose (Fig. 3). In the coarser grained and better-sorted L3 layer, there is neglectable Fe-oxide, and bleaching cannot be clearly indicated in fault zones. Layers L1–2 and L4-L7 are inherently red and bleaching easily identified. Grain size and pore filling clay content varies, with the interdune and sabkha samples offering high clay contents as seen in Fig. 3 for L2 and L4. Aeolian dune layers show less clay as seen in Fig. 3 for L6.

3. Methods

3.1. Field measurements

In-situ permeability by a Tiny-Perm II and rock hardness by Schmidt hammer type N were measured for various sedimentary facies and layers with a varying degree of bleaching within the footwall of the main fault. Measurements were performed both in the vertical direction (z), perpendicular to the sedimentary layering and in the horizontal direction (x,y) representing layer-parallel properties. The procedures for field measurements and calculations were adapted from (Alikarami et al., 2013). The Tiny-Perm II and Schmidt hammer values were used in empirical relations to calculate permeability and Young's modulus for selected layers, thereby defining a mechanical stratigraphy for the Entrada Sandstone succession. Results from these data represent the baseline for addressing variations related to migration pathways defined by bleaching.

Tiny-Perm II, a portable air permeameter, is used for measurements of rock matrix permeability on outcrops. The permeameter measurements are localized with a depth of investigation of less than four times the internal radius of the tip seal (Possemiers et al., 2012), providing an investigation depth of less than 18 mm for our Tiny-Perm II. Within fractured zones, we put the Tiny-Perm II on the intact portion of deformed rock with distance more than the investigation depth of Tiny-Perm II to the fractures. The equation provided by the user's manual of the instrument were applied to convert the Tiny-Perm II readings into permeability values

$$TP = -0.8206\log(K) + 12.8737 \qquad (1)$$

where TP is the Tiny-Perm II reading, and K is the permeability in mD. The recommended permeability measurement range is approximately from 10 mD to about 10 D by the manufacturer. For Tiny-Perm II readings, three measurements were performed on each measuring spot and the calculated average value was used for permeability calculations. The lower cut-off for measurements was set as 3 min, in line with the finding from Magnabosco et al. (2014), identifying a time constraint for when the measurements became unstable. Magnabosco et al. (2014) discuss the applicability of Miniperm for a drill core in tight sandstone and found a linear discrepancy of around one order of magnitude between Miniperm (2–25 mD) and plug measurements (0.01–2 mD) providing a correlation factor for their study. Our dataset includes measurements down to 5 mD and no calibration with plug measurements have been applied.

In-situ values of rock hardness have been measured by Schmidt Hammer type N. Based on rock mineralogy (sandstone) and hammer

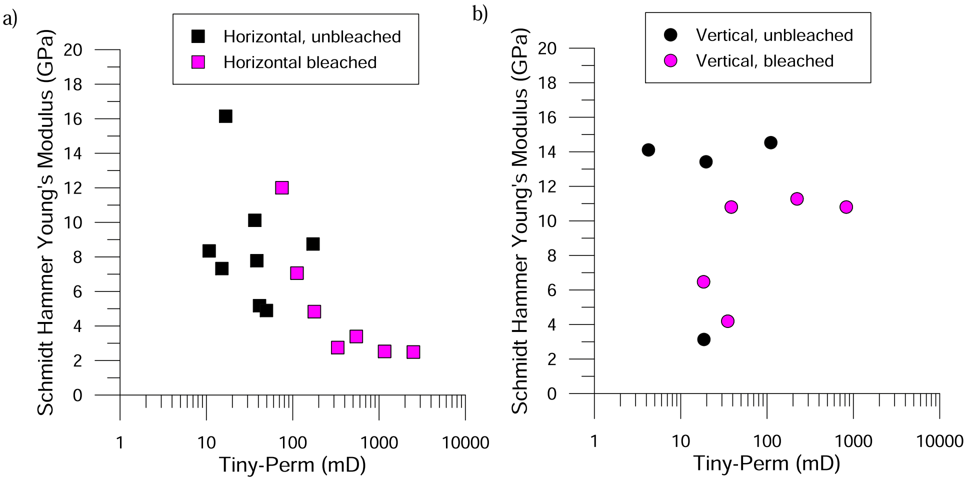

Fig. 5. Relationship between stiffness (Young's Modulus) and permeability for field measurements in the horizontal direction (a) and vertical direction (b). Horizontal permeability in bleached units is found to be highest, whereas the lowest permeability and highest stiffness are found for unbleached units.

type (N type), the empirical relation provided by Katz et al. (2000), Eqs. (2), is used to convert the Schmidt Hammer rebound values (HR) to Young's modulus E (GPa) to allow for comparison with data from the laboratory:

$$\ln(E) = -8.967 + 3.091\ln(HR) \pm 0.101\cdot\left(R^2 = 0.99\right) \qquad (2)$$

Schmidt hammer measurements have been acquired after the permeability measurements, on the same spots. The method of taking at least ten single impact readings, discarding those differing from the average by more than seven units, and averaging those left, as suggested by ASTM (2014a) has been followed in the study. Two angles for the readings were used, horizontal and vertical to identify anisotropy in the sedimentary layers, other inclinations for the measurements were avoided to minimize equipment angle effects in the readings (Aydin, 2008). The standard deviation for the recorded Schmidt Hammer rebound values (HR) are in the range of 1.1 to 3.8.

For field measurements, uncertainties related to near-surface weathering and irregularities was avoided for both measuremnts using a geological hammer to flatten and remove the upper weathered 1–3 cm of the rock and meet the requirements for an even and representative surface. Magnabosco et al. (2014) tested the reliability of the Tiny-Perm instrument on fresh rock (drill core), and could not identify any instrumental uncertainty as long as the seal between the nozzle and the substrata was good. Direct measurements on fractured areas were avoided. The measured properties are expected to represent average effective properties of the layers tested. Only silty to sandy layers with associated bleaching patterns are tested, the clay dominated units were not suitable for field testing or core sampling due to low permeability and more extensive weathering.

3.2. Lab analysis

3.2.1. Strength tests

Block samples from selected units were brought to the laboratory for analysis. Standard sized plugs of 25 mm diameter and around 55 mm height were prepared for the unconfined compressional strength (UCS) tests. For the Brazil tests discs of 25 mm diameter and height of 12.5 mm were used. UCS and indirect tensile strength using Brazil tests were performed according to ASTM standards (ASTM, 2014b; 2016) but with a different plug size as mentioned above due to sample constrains. The number of recommended tests to get representative values could not be fulfilled for all the sampled layers due to sample quality and integrity problems, as the rock was very fragile. UCS loading rates varied during the tests but were controlled to achieve failure 2–15 min after the start of loading. All plugs were tested in dry conditions. The porosity of the investigated layers was calculated from the plug bulk density and particle density. Since the layers all have a quartz-dominated mineralogy, the theoretical particle density of quartz (SiO_2), 2.65 g/cm^3, was used in the calculations. Static Young's Modulus E has been calculated from UCS test as the tangent modulus, E_{50}, at 50% of the maximum strength for the specimen.

3.2.2. Dynamic velocity measurements

The Ultrasonic analysis was conducted on oven-dried core-plug samples from outcrop using a portable device from Geotron Elektronik. Input parameters for P-wave and S-wave velocity measurements in this device are the bulk density and length of the samples measured in the laboratory. The dynamic Young's modulus of the rock is calculated from the measured velocities and density using empirical relations as explained in Torabi et al. (2018).

4. Results

4.1. Stratigraphic variations in mechanical and petrophysical properties

4.1.1. Layer variations in permeability and stiffness from field measurements

Measured rock hardness (converted to Young's Modulus) from Schmidt hammer and permeability from TinyPerm II for the reference log location 3 (Fig. 2) are presented for Layers L1-L7 inFig. 4. Permeability varies from 5 to 2500 mD, with the highest permeability recorded for layer L3. Horizontal permeability is 2–30 times higher than the vertical permeability with exception of L4 where horizontal permeability is half of the vertical permeability (Fig. 4). Young's Modulus is found to vary from 2 to16 GPa, with the lowest stiffness found for layer L3. Vertical Young's Modulus is on average 1.8 GPa higher than the horizontal Young's Modulus (Fig. 4). There are systematic variations between permeability, stiffness and bleaching (Fig. 5). A clear negative correlation between permeability and Young's modulus is found for the horizontal, layer parallel measurements. With increasing permeability, Young's modulus decreases and vice versa (Fig. 5a). This trend is less pronounced for the vertical, layer perpendicular measurements (Fig. 5b), where less data points are available due to very low none-measurable vertical permeability for some layers. Layers with permeability above 200 mD are all bleached and cluster towards the low stiffness. L3 appears as light coloured throughout the study area, indicating that relict fluid migration could be difficult to identify, despite this being a very conductive unit. In layers with high stiffness and low permeability L1-L2 and L4-L5, bleaching is less common and the red

Table 2
Strength and E modulus from UCS tests, Brazil tests and velocity measurements.

Layer	Bleaching	# Brazil	# UCS	Average plug porosity (%)	Average tensile strength (MPa)	Average UCS strength (MPa)	Average Static Young's Modulus, E (GPa)	Dynamic Young's modulus, E (GPa)
L7$_{upper}$	no	10	6	12.93	1.77	33.8	3.66	
L7$_{upper}$	no			19.7				4.9
L6$_{upper}$	yes	10	6	18.46	1.13	19.66	2.15	
L6$_{upper}$	yes			22.35				1.8
L6$_{lower}$	no	9	6	8.57	3.94	62.00	8.24	
L5	no			15.19				7.87
L4	no	18	4	14.37	1.63	37.87	2.77	
L3$_{upper}$	yes			19.79				14.62
L3$_{lower}$	yes	16	2	28.56	0.41	2.13	0.16	
L3$_{lower}$	yes			18.22				4.99
L2	no	17	–	18.24	1.23			
L2	no			11.74				8.8
L1	no	9	4	8.54	2.63	65.08	4.95	
L1	no			10.25				13.42

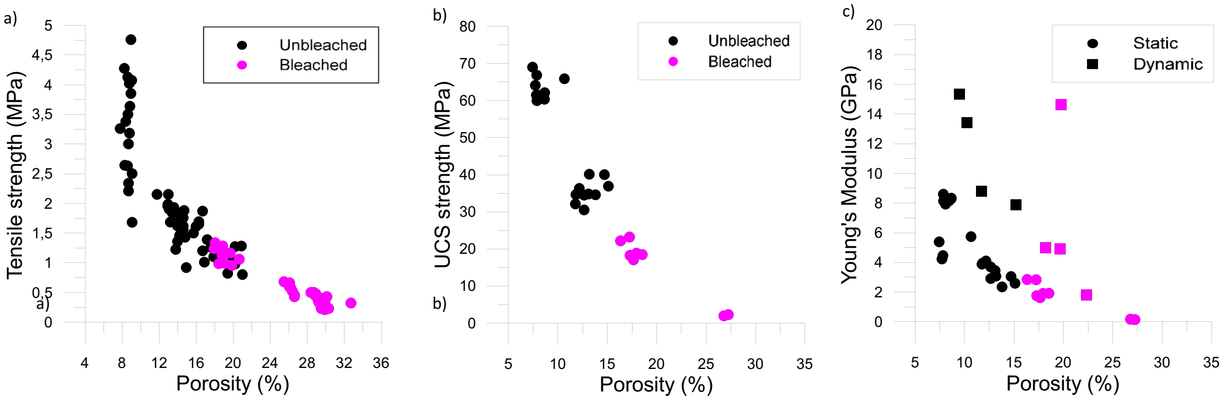

Fig. 6. Tensile strength (a) and UCS strength (b) and Young's Modulus (c) versus porosity for vertical plugs from all layers. The data separates between plugs from bleached (pink) and unbleached layers (black). Dataset based on MSc theses work (Kristensen, 2017; E B Larsen, 2015).

staining well preserved.

4.1.2. *Layer variations in porosity and mechanical strength from plug measurements*

For the experimental results, measured tensile strength is found to vary from 0.4 to 4 MPa, whereas the average UCS strength varies from 2 to 65 MPa. Static Young's Modulus is ranging from 0.16 to around 8 GPa, and dynamic Young's Modulus range from 1.8 to 14.62 GPa (Table 2). Both tensile and UCS strength are increasing with decreasing porosity, although for the lowest porosities the spread in tensile strength is high compared to the more porous plugs. When considering bleaching effect in the plots (Fig. 6), data from bleached layers show systematic lower strength. The static Young's Modulus calculated from UCS and the dynamic Young's Modulus from velocity tests are compared in Fig. 6c and show a good correlation between strength and porosity (possibly with the exception of one L3 sample that has a relative high modulus for the high porosity measured). It is also clear that the dynamic Young's Modulus is slightly higher than the static modulus in line with relationships comparing static and dynamic properties (e.g. Zoback, 2010). Both datasets indicate a negative linear correlation between porosity and stiffness. Measurements on bleached samples show higher porosity and lower stiffness, whereas unbleached samples show lower porosity and higher stiffness.

4.2. *Bleaching related variations in mechanical and petrophysical properties*

4.2.1. *Layer parallel bleaching inside and outside the fault damage zone*

The bleaching observed along layers L6 and L7 varies over the outcrop. The most intense bleaching appears in location 2, within the main fault damage zone. L6 is fully bleached over the 1.7 m layer thickness, while L7 that is 2.5 m thick has a very distinct bleaching in the lower 0.7 m (Fig. 7a). The layers L6 and L7 have a bed boundary that displays slight changes in average grain size. Further, this boundary hosts a fracture in parts of the study area. The layer parallel bleaching fades out with distance from the fault. In location 3 the bleaching is less intense, and the thickness of the bleached zone is reduced to 20–30 cm. Hence, in this area bleaching covers less than the layer thickness both for L6 and L7 (Fig. 7b and c).

Comparing the petrophysical and mechanical properties for layers L6 and L7, the fault damage zone of location 2 and host-rock of location 3 offer a higher permeability for the bleached versus unbleached layers (Fig. 7). Similarly, stiffness and strength are lower for bleached versus unbleached layers (Fig. 7). In the fault damage zone, permeability of bleached layers is lower compared to outside the fault zone, although the bleaching is more extensive in this area (Fig. 7a, b). Horizontal stiffness is similar for the two locations, whereas the vertical stiffness is lower within the fault damage zone (location 2) compared to outside the fault zone (location 3).

4.2.2. *Strength and permeability changes across bleached fractures*

Bleached fractures are parallel to subparallel to the main fault orientation and are mostly observed on bedding surfaces. Bleaching appears as an undulating halo around fractures that varies from only a few mm to 30 cm in width, sporadically reaching 1 m width (Fig. 8a). Systematic measurements of permeability and stiffness of fractures in layer L1 (location 1) and L4 (location 2) for a total of 18 fractures show no systematic difference in properties between the bleached halo and

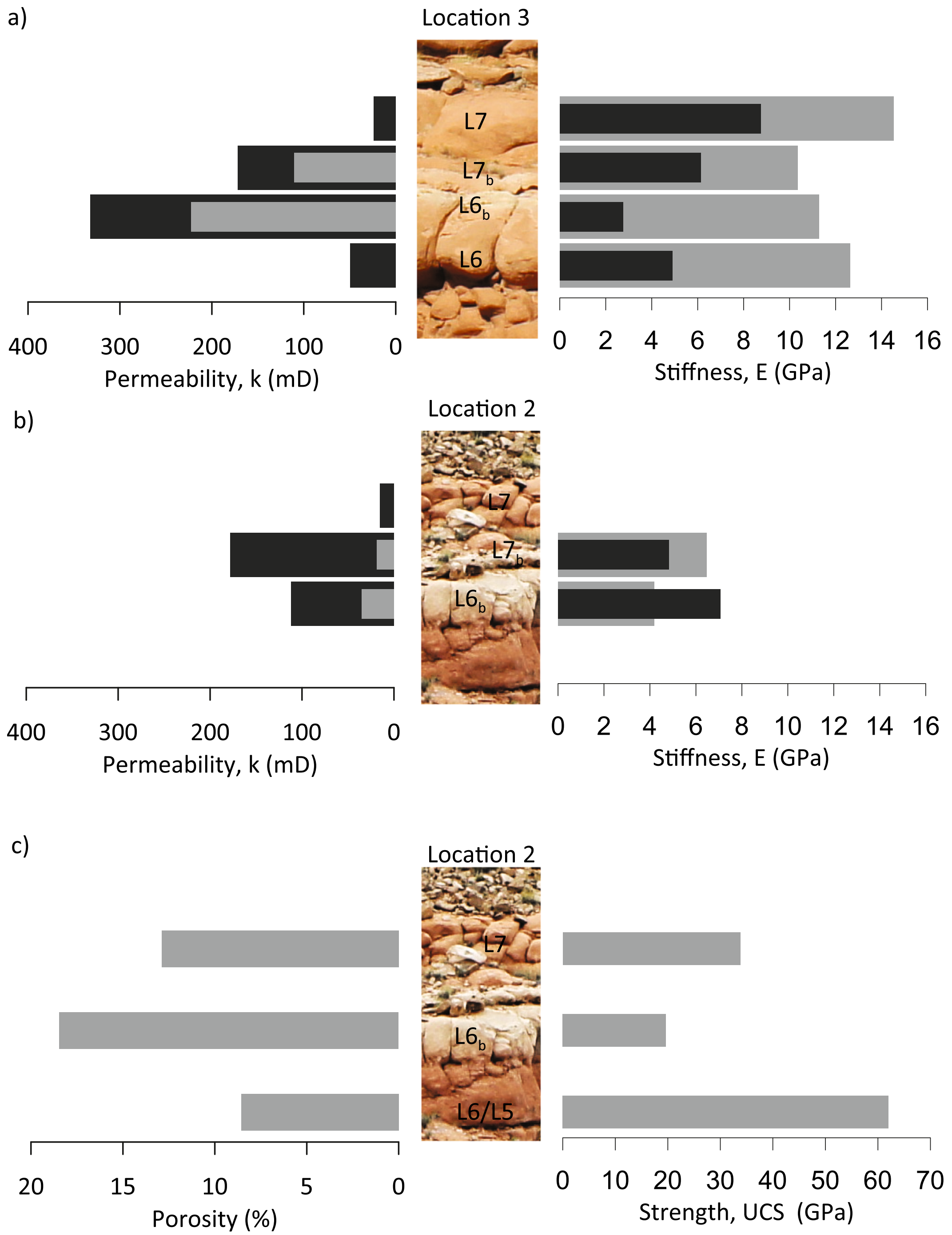

Fig. 7. Comparison of petrophysical and mechanical properties for the partly bleached L6 and L7 outside the fault damage zone (location 3) and within the fault damage zone (location 2). Black bars are for horizontal direction and grey bars are for the vertical direction. $L6_b$ and $L7_b$ denotes the bleached parts of the layer L6 and L7. a) Permeability and stiffness for location 3. b) Permeability and stiffness for location 2. c) Porosity and strength for location 2.

the host rock outside the halos (Fig. 8b). No difference in apparent weathering is recorded between the bleached and unbleached zones, supporting low impact of bleaching on the petrophysical properties.

5. Discussion

The mechanical and petrophysical properties measured provide information on the present-day properties for the studied sedimentary succession, whereas the bleaching patterns are considered an excellent example of ancient fluid migration pathways (e.g. Kampman et al., 2014; Ogata et al., 2014; Parry et al., 2004). This means that the measured absolute values for mechanical and petrophysical properties are not necessarily representative for the time of the fluid circulation, fracturing and bleaching, as the area has a complex geological history with several deformation events and different fluid mixtures circulating, some diagenetic imprints may post-date the main bleaching event (Rushton et al., 2020; Skurtveit et al., 2020). However, the relative changes in mechanical and petrophysical properties are related to the sedimentary facies and of relevance for understanding the bleaching patterns and associated fluid distribution.

Along the vertical sedimentary section presented in Fig. 4, mechanical stratigraphy is expressed by layering with variable measured

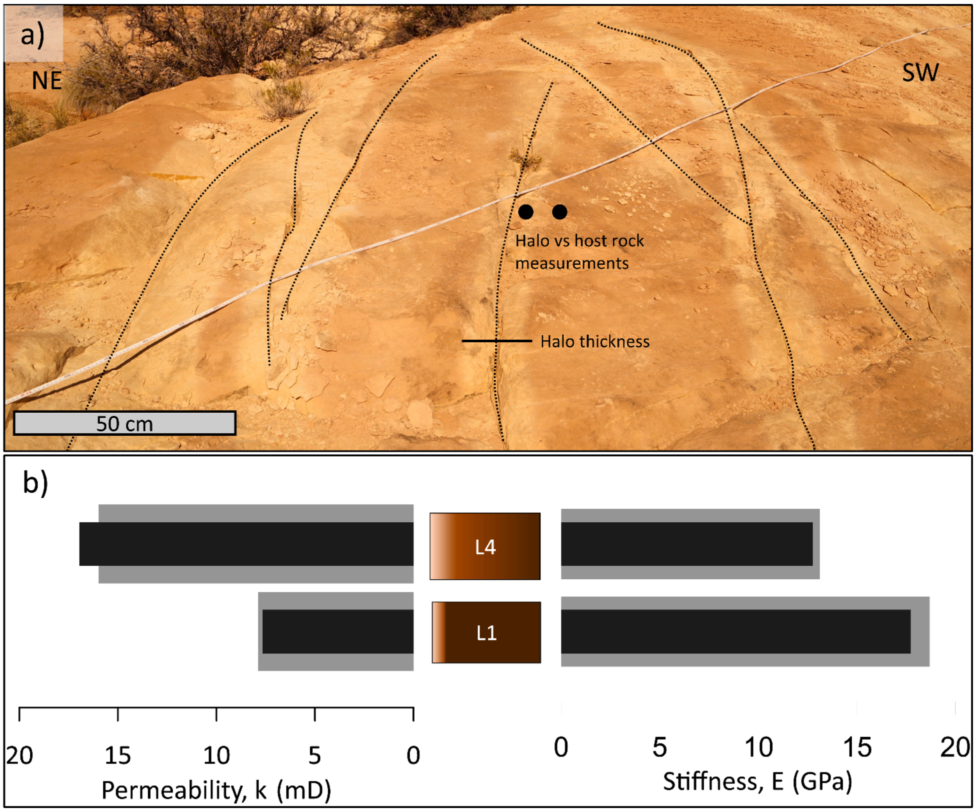

Fig. 8. a) Example of bleached haloes around fractures in layer L4 in the damage or process zone of the main fault (location 2). b) Statistical average permeability and stiffness for 11 fractures in layer L4 and 7 fractures in layer L1 showing no distinct difference for the bleached versus unbleached rock. Black bars are for the unbleached host rock whereas grey bars are from the bleached fracture halos. Dataset based on MSc thesis, Kristensen (2017).

properties. With increasing permeability, the Young's modulus decreases in different layers and vice versa (Fig. 5). This is in line with previous studies that show a similar correlation between permeability and Young's modulus estimates from TinyPerm II and Schmidt Hammer readings in the field (e.g. Alikarami et al., 2013; Torabi et al., 2020). This is further substantiated by the strong negative correlation between porosity and strength of the rock layers based on the static and dynamic laboratory measurements as presented in Fig. 6. Hence, bleaching of layers is associated with higher porosity and permeability and lower strength/stiffness, with trends signifying changes in grain size and the distribution of cement and bleaching in different layers as observed in the field and during petrographic analysis. A threshold for bleaching occurs at 16–17% porosity, as no layers with lower porosity display continuous bleaching (Fig. 6), corresponding to vertical permeability of 10 mD and horizontal permeability of 200 mD (Fig. 5). For layers with lower porosity and permeability no distinct bleaching can be observed unless associated with layer perpendicular fractures hosting bleaching haloes within the fault damage zone (Torabi et al., 2019a) or within fracture swarms associated with minor faults and tip zones (Ogata et al., 2014).

Our observations verify that layer parallel fluid migration identified by bleaching focus towards high porosity and permeability sedimentary layers, L3, L6 and L7, all representing sandy facies, like aeolian dunes, tidal bars or fluvial channels. Of these three layers, L3 has a different

Table 3
Deformation frequencies for various layers and locations based on measurements reported in MSc thesis (Hope, 2015; Kristensen, 2017; E B Larsen, 2015) and literature (Torabi et al., 2019a).

Scanline layer	Location	Bleaching	Fracture average, maximum (#/metre)	Deformation band average, maximum (#/metre)	Comment	Reference
L6	2	Bleached	2, 5	3, 8	54.5 m scanline	(Torabi et al., 2019a)
L5	2	Partly bleached	4, 10	no	53 m scanline	(Torabi et al., 2019a)
L4	2	Partly bleached	4, 9	0.07, 2	54 m scanline	(Torabi et al., 2019a)
L4	1	unbleached	0.8, 4	no	10 m scanline across minor fault	(*Larsen*, 2015)
L3	1	Bleached	0.3, 2	1.5, 3	10 m scanline across minor fault	(*Larsen*, 2015)
L3	1,3	Bleached	no	1.5, 18	Several scanlines in L3	(*Hope*, 2015)
L2	1	unbleached	2, 4	Some	10 m scanline across minor fault	(*Larsen*, 2015)
L1	1	unbleached	2.5, 5	no	10 m scanline across minor fault	(*Larsen*, 2015)
L1	1	unbleached	1.7, 4	no	10 m	(*Kristensen*, 2017)

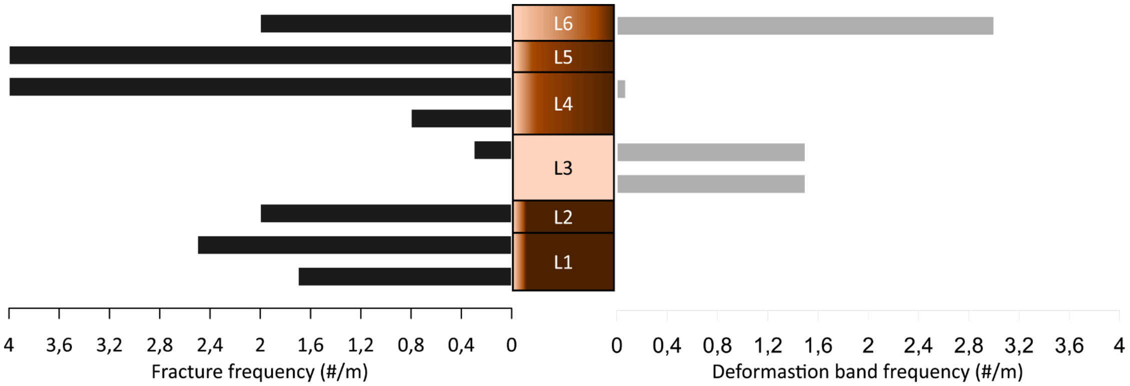

Fig. 9. Average deformation bands and fracture frequencies for bleached, non-bleached and partly bleached layers from location listed in Table 3.

mineralogy, grain size and sorting (Table 1, Fig. 3) and generally lack residual Fe-oxides. Interpretations of depositional environment (Table 1), lack of clay-fraction porefill and the observed, pervasive light colour suggest that this layer was not inherently stained red. This is in line with observations from other parts of the SRS area (Bromander, 2018; Hope, 2015). However, the high permeability suggests that the layer has been transporting bleaching fluids, as evident from diffusive, bleached rims in over- and underlying red units (Fig. 2). For the layers L6 and L7, bleaching is most intense in the fault damage zone (location 2) and fading with distance from the fault (location 3), as seen in Fig. 7. Bleaching diminishes away from the fault signifies along-fault fluid flow as a source for reducing fluids entering the layers. Further, the bleaching of location 3 is pronounced at the top of L6 and at the base of L7 suggesting that the recorded fracture along the layer interface contributed to flow out from the fault zone. Few contributions address fluid transport on fractures along bedding interfaces (Larsen and Gudmundsson, 2010; Larsen et al., 2010), especially for siliciclastic units, but bedding parallel veins are common in a number of sedimentary basins.

Fracture and deformation band frequency data have previously been collected from Humbug Flats in several studies (Ogata et al., 2014; Torabi et al., 2019a) and MSc theses (Hope, 2015; Kristensen, 2017; Larsen, 2015). These records are aligned with the layers presented in this study (Table 3). Average fracture and deformation band frequencies plotted for all layers in Fig. 9 show that layers ascribed the highest porosity (L3 and L6) are dominated by deformation bands. This is in line with our understanding of deformation mechanisms for material with high porosity forming deformation bands (Skurtveit et al., 2013; Torabi et al., 2019a; Torabi and Zarifi, 2014). Characteristic for L3 deformation band distribution is the high abundance of bands observed in location 1 and 3, outside the main fault damage zone, attributed to a collapse of the reservoir (Hope, 2015). Similar, layer specific collapse of L3 is also observed in other parts of the SRS (Bromander, 2018). The upper part of L6 show both deformation bands and fractures linked to porosity ranging from 18 to 22% for the bleached samples close to the main fault (location 2). On the contrary, for red-stained parts of L6, porosities below 10% were measured, and no deformation bands observed. The red-stained and locally bleached layers (L1, L2, L4 and L5) host mainly fractures, with the higher fracture frequencies observed for scanlines in location 2, near the main fault defining the inner and outer damage zone of the fault (Torabi et al., 2019a).

Although the bleaching observed for the stratigraphic section in (Fig. 4) is clearly associated with lower strength, there is no clear indication for reduced strength due to bleaching and removal of Fe-oxides. The higher porosity and permeability measured for the same layers suggest that the bleaching is facies controlled, with permeable facies favouring flow of reducing fluid in the specific units during transient fluid events (Newell et al., 2019). The facies control on fluid circulation is supported by the lack of change in material properties for bleached halos around fractures where no change in properties could be measured between the bleached halo and surrounding rock within the same facies (Fig. 8). However, studies on CO_2 alteration of mechanical properties have shown reduction in shear strength and stiffness (Espinoza et al., 2018) and fracture toughness (Major et al., 2018). In order to consider bleaching and the potential for mechanical weakening, the fluid transport properties should be considered (Skurtveit et al., 2018). Both advective and diffusive transport of Fe is possible and very small amounts of Fe-oxide/hydroxide contents are needed to cause red staining of sediment (Beitler et al., 2005). Advective transport as cause for bleaching requires very large fluid volumes (Parry et al., 2004), whereas long residence time and pressure in fractures and porous layers allows for diffusive bleaching into less permeable units (Newell et al., 2019; Sundal et al., 2017). High fluid flux may be possible for highly permeable facies, but also during processes such as seismic venting, advective transport may be significant along fault slip surfaces as a transient event. On the other hand, diffusive bleaching through Fe-reduction may be the most efficient at a local scale around fractures and for layers outside the main fault zone. The inability for the field measurements to identify weakening for bleached fracture halos (Fig. 8) can be explained by diffusive bleaching of the rock and potential advective transport only along the fracture aperture. The very small amount of Fe-oxide needed to cause red staining (Beitler et al., 2005) indicate a potential for bleaching without changing the material properties significantly as observed for the fractured halos.

6. Conclusion

Our work documents that bleaching patterns along a faulted succession provide insight into fluid migration pathways along fault zones. Besides, along-fault fluid flow cause layer-parallel sweep into parts of the local stratigraphy dictated by bed properties and in places fractures along bedding interfaces.

The main findings of this study are:

- For the mechanical stratigraphy within the Entrada Sandstone, strong correlations exist between permeability and stiffness, as well as between porosity and strength. Permeability is increasing with decreasing stiffness and porosity is increasing with decreasing strength. Bleaching is associated with high porosity and high permeability layers, implying a sedimentary facies control on the potential for pervasive bleaching along these layers.
- Deformation structures conform to mechanical stratigraphy, where stiff and low porosity layers host fractures, while weaker porous layers are dominated by deformation bands.
- The most intense layer parallel bleaching appears proximal to faults and fades out with distance from the main slip surface suggesting that the fault provides the source for the reducing fluid.
- Bleaching patterns identifies fractures in the damage zone of the analysed fault as important conduits for vertical flow across low

permeable and stiff layers, whereas permeable layers offer layer-parallel sweep out from the fault.

- A new observation is that fractures on bed interfaces contribute to flow away from the fault zone causing fluid transport and bleaching outside the main fault zone.
- No detectable differences in mechanical strength nor permeability are observed between inherently red stained host rock and within local diffusive bleaching haloes along fractures.
- Layer parallel flow out form the fault dominate in the more porous and permeable facies implying preferential fluid migration in these layers due to the petrophysical properties of the rock. Layer weakening and/or permeability changes caused by the Fe-oxides removal or other fluid alteration processes for these layers cannot be quantified in the current study.
- The findings suggest that local mechanical and petrophysical stratigraphy plays an important role in controlling both the layer parallel fluid sweep out from the fault as well as cross layer fracture flow.

CRediT authorship contribution statement

E. Skurtveit: Methodology, Investigation, Writing – original draft. **A. Torabi:** Methodology, Investigation, Writing – original draft. **A. Sundal:** Methodology, Investigation, Writing – original draft. **A. Braathen:** Conceptualization, Writing – review & editing, Funding acquisition.

Declaration of Competing Interest

The authors declare that they have no known competing financial interests or personal relationships that could have appeared to influence the work reported in this paper.

Acknowledgment

Funding for the research is awarded from the Research Council of Norway (RCN) through the CO_2 Seal Bypass and COTEC projects (RCN# 244049, 295061), with recent incentives offered by the NCCS Centre (RCN# 257579) and FRISK project (RCN# 294719). Contributions by Ida Hope, Eivind B. Larsen, Runar S. Kristensen, Nikoline Bromander and Sigrid Ø. Da Costa are acknowledged. We also like to thank our three reviewers for positive and constructive input on the manuscript.

References

Alikarami, R., Torabi, A., Kolyukhin, D., Skurtveit, E., 2013. Geostatistical relationships between mechanical and petrophysical properties of deformed sandstone. Int. J. Rock Mech. Min. Sci. 63, 27–38.

ASTM, 2014a. ASTM D5873-14, Standard Test Method for Determination of Rock Hardness By Rebound Hammer Method, Edited. ASTM International, West Conshohocken, PA. https://doi.org/10.1520/D5873-14.

ASTM, 2014b. ASTM D7012-14e1, Standard test Method For Compressive Strength and Elastic Moduli of Intact Rock Core Specimens Under Varying States of Stress and temperatures, Edited. ASTM International, West Conshohocken, PA. https://doi.org/10.1520/D7012-14E01.

ASTM, 2016. ASTM D3967-16, Standard Test Method for Splitting Tensile Strength of Intact Rock Core Specimens, Edited. ASTM International, West Conshohocken, PA. https://doi.org/10.1520/D3967-16.

Aydin, A., 2008. ISRM suggested method for determination of the Schmidt hammer rebound hardness: revised version. The ISRM Suggested Methods For Rock Characterization, Testing and Monitoring: 2007-2014, Edited. Springer, pp. 25–33.

Beitler, B., Parry, W.T., Chan, M.A., 2005. Fingerprints of fluid flow: chemical diagenetic history of the Jurassic Navajo Sandstone, southern Utah, USA. J. Sediment. Res. 75 (4), 547–561.

Bromander, N., 2018. Facies-controlled Reservoir Quality and Preferential Deformation in Sandstone reservoirs; a Case Study from the Entrada Sandstone. University of Oslo, Utah, USA.

Braathen, A., Tveranger, J., Fossen, H., Skar, T., Cardozo, N., Semshaug, S., Bastesen, E., Sverdrup, E., 2009. Fault facies and its application to sandstone reservoirs. Am. Assoc. Pet Geol. Bull. 93 (7), 891–917.

Bump, A.P., Davis, G.H., 2003. Late Cretaceous-early Tertiary Laramide deformation of the northern Colorado Plateau, Utah and Colorado. J. Struct. Geol. 25 (3), 421–440. https://doi.org/10.1016/s0191-8141(02)00033-0.

Burnside, N.M., Shipton, Z.K., Dockrill, B., Ellam, R.M., 2013. Man-made versus natural CO2 leakage: a 400 ky history of an analogue for engineered geological storage of CO2. Geology 41 (4), 471–474.

Chan, M.A., Parry, W., Bowman, J., 2000. Diagenetic hematite and manganese oxides and fault-related fluid flow in Jurassic sandstones, southeastern Utah. Am. Assoc. Pet Geol. Bull. 84 (9), 1281–1310.

Da Costa, S.Ø., 2018. The Complexity of Regional erosion; incision, faulting, and Deposition During the Development of the J-3 Unconformity. University of Oslo, Utah, USA.

edited by Davis, G.H., Bump, A.P., 2009. Structural geologic evolution of the Colorado Plateau. In: Kay, S., Ramos, V., Dickinson, W. (Eds.), Backbone of the Americas: Shallow Subduction, Plateau Uplift, and Ridge and Terrane Collision. Geological Society of America, pp. 99–124. edited by.

Doelling, H.H. (2002), Interim geologic map of the San Rafael Desert 30′ x 60′ quadrangle, Emery and Grand Counties, Utah: Utah Geological Survey Open-File Report, 404, 20.

Eichhubl, P., Davatz, N.C., Becker, S.P., 2009. Structural and diagenetic control of fluid migration and cementation along the Moab fault, Utah. Am. Assoc. Pet Geol. Bull. 93 (5), 653–681.

Espinoza, D.N., Jung, H., Major, J.R., Sun, Z., Ramos, M.J., Eichhubl, P., Balhoff, M.T., Choens, R.C., Dewers, T.A., 2018. CO2 charged brines changed rock strength and stiffness at Crystal Geyser, Utah: implications for leaking subsurface CO2 storage reservoirs. Int. J. Greenhouse Gas Control 73, 16–28.

Fachri, M., Tveranger, J., Braathen, A., Røe, P., 2016. Volumetric faults in field-sized reservoir simulation models: a first case study. Am. Assoc. Pet Geol. Bull. 100 (5), 795–817.

Faille, I., Thibaut, M., Cacas, M.-.C., Havé, P., Willien, F., Wolf, S., Agélas, L., Pegaz-Fiornet, S., 2014. Modeling fluid flow in faulted basins. Oil & Gas Science and Technology–Revue d'IFP Energies nouvelles 69 (4), 529–553.

Faulkner, D., Jackson, C., Lunn, R., Schlische, R., Shipton, Z.K., Wibberley, C., Withjack, M., 2010. A review of recent developments concerning the structure, mechanics and fluid flow properties of fault zones. J. Struct. Geol. 32 (11), 1557–1575.

Ferrill, D.A., Morris, A.P., McGinnis, R.N., Smart, K.J., Wigginton, S.S., Hill, N.J., 2017. Mechanical stratigraphy and normal faulting. J. Struct. Geol. 94, 275–302.

Frery, E., Gratier, J.-.P., Ellouz-Zimmerman, N., Loiselet, C., Braun, J., Deschamps, P., Blamart, D., Hamelin, B., Swennen, R., 2015. Evolution of fault permeability during episodic fluid circulation: evidence for the effects of fluid–rock interactions from travertine studies (Utah–USA). Tectonophysics 651, 121–137.

Garden, I., Guscott, S., Burley, S., Foxford, K., Walsh, J., Marshall, J., 2001. An exhumed palaeo-hydrocarbon migration fairway in a faulted carrier system, Entrada Sandstone of SE Utah, USA. Geofluids 1 (3), 195–213.

Hope, I., 2015. Deformation Bands in Collapsed Sandstone reservoirs, An example from Upper Jurassic Entrada Formation. University of Oslo, Utah, USA.

Kampman, N., Bickle, M., Maskell, A., Chapman, H., Evans, J., Purser, G., Zhou, Z., Schaller, M., Gattacceca, J.C., Bertier, P., 2014. Drilling and sampling a natural CO 2 reservoir: implications for fluid flow and CO 2-fluid–rock reactions during CO 2 migration through the overburden. Chem. Geol. 369, 51–82.

Kampman, N., Busch, A., Bertier, P., Snippe, J., Hangx, S., Pipich, V., Di, Z., Rother, G., Harrington, J., Evans, J.P., 2016. Observational evidence confirms modelling of the long-term integrity of CO 2-reservoir caprocks. Nat. Commun. 7 (1), 1–10.

Katz, O., Reches, Z., Roegiers, J.-.C., 2000. Evaluation of mechanical rock properties using a Schmidt Hammer. Int. J. Rock Mech. Min. Sci. 37 (4), 723–728.

Knipe, R., 1997. Juxtaposition and seal diagrams to help analyze fault seals in hydrocarbon reservoirs. Am. Assoc. Pet Geol. Bull. 81 (2), 187–195.

Kristensen, R.S., 2017. Geomechanical and Petrophysical Properties of Fractured Siliciclastic Rocks and Its Implications For CO2 Storage. University of Bergen.

Larsen, B., Gudmundsson, A., 2010. Linking of fractures in layered rocks: implications for permeability. Tectonophysics 492 (1–4), 108–120.

Larsen, B., Gudmundsson, A., Grunnaleite, I., Sælen, G., Talbot, M.R., Buckley, S.J., 2010. Effects of sedimentary interfaces on fracture pattern, linkage, and cluster formation in peritidal carbonate rocks. Mar. Pet. Geol. 27 (7), 1531–1550.

Larsen, E.B., 2015. Geomechanical and Structural characteristics of a Paleoreservoir-Caprock sucsession; Sandstones of Humbugflats. Central Utah, University of Oslo.

Lunn, R.J., Shipton, Z.K., Bright, A.M., 2008. How can we improve estimates of bulk fault zone hydraulic properties? Geol. Soc., Lond., Spec. Publ. 299 (1), 231–237.

Magnabosco, C., Braathen, A., Ogata, K., 2014. Permeability model of tight reservoir sandstones combining core-plug and Miniperm analysis of drillcore; Longyearbyen CO2 Lab, Svalbard. Norw. J. Geol. 94, 189–200.

Major, J.R., Eichhubl, P., Dewers, T.A., Olson, J.E., 2018. Effect of CO2–brine–rock interaction on fracture mechanical properties of CO2 reservoirs and seals. Earth Planet. Sci. Lett. 499, 37–47.

Newell, A.J., Pourmalek, A., Butcher, A.S., Shariatipour, S.M., 2019. The importance of lithofacies control on fluid migration in heterogeneous aeolian formations for geological CO2 storage: lessons from observational evidence and modelling of bleached palaeoreservoirs at Salt Wash Graben, Utah. Int. J. Greenhouse Gas Control 91, 102841.

Ogata, K., Senger, K., Braathen, A., Tveranger, J., 2014. Fracture corridors as seal-bypass systems in siliciclastic reservoir-cap rock successions: field-based insights from the Jurassic Entrada Formation (SE Utah, USA). J. Struct. Geol. 66 (0), 162–187. https://doi.org/10.1016/j.jsg.2014.05.005.

Parry, W., Chan, M.A., Beitler, B., 2004. Chemical bleaching indicates episodes of fluid flow in deformation bands in sandstone. Am. Assoc. Pet. Geol. Bull. 88 (2), 175–191.

Pei, Y., Paton, D.A., Knipe, R.J., Wu, K., 2015. A review of fault sealing behaviour and its evaluation in siliciclastic rocks. Earth Sci. Rev. 150, 121–138.

Petrie, E.S., Evans, J.P., Bauer, S., 2014. Failure of cap-rock seals as determined from mechanical stratigraphy, stress history, and tensile-failure analysis of exhumed analogsStress History and Tensile Failure Analysis of Exhumed Caprock Seal Analogs. Am. Assoc. Pet. Geol. Bull. 98 (11), 2365–2389.

Possemiers, M., Huysmans, M., Peeters, L., Batelaan, O., Dassargues, A., 2012. Relationship between sedimentary features and permeability at different scales in the Brussels Sands. Geologica Belgica.

Rushton, J.C., Wagner, D., Pearce, J.M., Rochelle, C.A., Purser, G., 2020. Red-bed bleaching in a CO2 storage analogue: insights from Entrada Sandstone fracture-hosted mineralization. J. Sediment. Res. 90 (1), 48–66.

Skurtveit, E., Braathen, A., Larsen, E.B., Sauvin, G., Sundal, A., Zuchuat, V., 2017. Pressure Induced Deformation and Flow Using CO2 Field Analogues, Utah. Energy Procedia 114, 3257–3266. https://doi.org/10.1016/j.egypro.2017.03.1457.

edited by Skurtveit, E., Miri, R., Hellevang, H., 2018. Fluid-Rock Interactions in Clay-Rich Seals: impact on Transport and Mechanical Properties. In: Vialle, S., Li, Y., Carey, J.W. (Eds.), Geological Carbon Storage: Subsurface Seals and Caprock Integrity. John Wiley & Sons, p. 167. edited by.

Skurtveit, E., Sundal, A., Bjørnarå, T.I., Soldal, M., Sauvin, G., Zuchuat, V., Midtkandal, I., Braathen, A., 2020. Experimental investigation of natural fracture stiffness and flow properties in a faulted CO2 bypass system (Utah, USA). J. Geophys. Res. 125 (7), e2019JB018917.

Skurtveit, E., Torabi, A., Gabrielsen, R.H., Zoback, M.D., 2013. Experimental investigation of deformation mechanisms during shear-enhanced compaction in poorly lithified sandstone and sand. J. Geophys. Res. 118 (8), 4083–4100. https://doi.org/10.1002/jgrb.50342.

Sundal, A., Miri, R., Hellevang, H., Tveranger, J., Midtkandal, I., Zuchuat, V., Aagaard, P., Braathen, A., 2017. Movement of CO2 charged fluids in low permeability rocks during deformation: migration patterns in the Carmel Formation, Utah. Energy Procedia 114, 4537–4544.

Sundal, A., Skurtveit, E., Midtkandal, I., Hope, I., Larsen, E., Kristensen, R., Braathen, A., 2016. Facies-controlled fluid migration patterns and subsequent reservoir collapse by depressurization-the Entrada Sandstone, Utah. In: paper presented at AGU Fall Meeting Abstracts.

Torabi, A., Alaei, B., Ellingsen, T.S.S., 2018. Faults and fractures in basement rocks, their architecture, petrophysical and mechanical properties. J. Struct. Geol. 117, 256–263.

Torabi, A., Ellingsen, T.S.S., Johannessen, M.U., Alaei, B., Rotevatn, A., Chiarella, D., 2019a. Fault zone architecture and its scaling laws: where does the damage zone start and stop? Geol. Soc., Lond., Spec. Publ. 496. SP496-2018-2151.

Torabi, A., Jiménez-Millán, J., Jiménez-Espinosa, R., García-Tortosa, F.J., Abad, I., Ellingsen, T.S.S., 2020. Effect of Mineral Processes and Deformation on the Petrophysical Properties of Soft Rocks during Active Faulting. Minerals 10 (5), 444. https://doi.org/10.3390/min10050444.

Torabi, A., Johannessen, M.U., Ellingsen, T.S.S., 2019b. Fault Core Thickness: insights from Siliciclastic and Carbonate Rocks. Geofluids 2019.

Torabi, A., Zarifi, Z., 2014. Energy release rate of propagating deformation bands and their hosted cracks. Int. J. Rock Mech. Min. Sci. 67 (0), 184–190. https://doi.org/10.1016/j.ijrmms.2013.10.007.

Wigley, M., Kampman, N., Dubacq, B., Bickle, M., 2012. Fluid-mineral reactions and trace metal mobilization in an exhumed natural CO2 reservoir, Green River, Utah. Geology 40 (6), 555–558.

Zoback, M.D., 2010. Reservoir Geomechanics. Cambridge University Press, p. 449.

Zuchuat, V., Midtkandal, I., Poyatos-Moré, M., Da Costa, S., Brooks, H.L., Halvorsen, K., Cote, N., Sundal, A., Braathen, A., 2019. Composite and diachronous stratigraphic surfaces in low-gradient, transitional settings: the J-3 “unconformity” and the Curtis Formation, east-central Utah, USA. J. Sediment. Res. 89 (11), 1075–1095.